

Materials Advances

Accepted Manuscript

This article can be cited before page numbers have been issued, to do this please use: X. Yang, M. Alhabradi, A. Roy, M. Alruwaili, D. Benson, H. Chang, X. Li, A. A. Tahir and Y. Zhu, *Mater. Adv.*, 2026, DOI: 10.1039/D5MA01065A.



This is an Accepted Manuscript, which has been through the Royal Society of Chemistry peer review process and has been accepted for publication.

Accepted Manuscripts are published online shortly after acceptance, before technical editing, formatting and proof reading. Using this free service, authors can make their results available to the community, in citable form, before we publish the edited article. We will replace this Accepted Manuscript with the edited and formatted Advance Article as soon as it is available.

You can find more information about Accepted Manuscripts in the [Information for Authors](#).

Please note that technical editing may introduce minor changes to the text and/or graphics, which may alter content. The journal's standard [Terms & Conditions](#) and the [Ethical guidelines](#) still apply. In no event shall the Royal Society of Chemistry be held responsible for any errors or omissions in this Accepted Manuscript or any consequences arising from the use of any information it contains.

1 **Enhancing the Uniformity of CuBi₂O₄ Thin Film for Photoelectrochemical (PEC)**
2 **Water Splitting through Urea-Modified Ethylene Glycol Electrolyte**

3 Xiuru Yang^a, Mansour Alhabradi^{bc}, Anurag Roy^b, Manal Alruwaili^{bd}, David Benson^b, Hong
4 Chang^a, Xiaohong Li^b, Asif Ali Tahir*^b, Yanqiu Zhu*^a

5 *Corresponding authors

6 ^a Faculty of Environment, Science and Economy, University of Exeter, Exeter EX4 4QF, UK

7 ^b Faculty of Environment, Science and Economy, University of Exeter, Penryn TR10 9FE, UK

8 ^c Department of Physics, Faculty of Science, Majmaah University, Majmaah, 11952, Saudi
9 Arabia

10 ^d Department of Physics, Faculty of Science, Jouf University, 2014, Sakaka 42421, Saudi
11 Arabia

12 E-mail: Y.Zhu@exeter.ac.uk

13

14



1 **Abstract**

2 CuBi₂O₄ photocathode with interconnected nanoparticle textured morphology has reached a
3 photocurrent density of -0.94 mA/cm² at 0.52 V vs. RHE. It was successfully fabricated via
4 electrodeposition using ethylene glycol (EG) containing a specific concentration of
5 Bi(NO₃)₃·5H₂O and CuCl₂ as the electrolyte, followed by 2 h of calcination at 550 °C. Using
6 urea as a complexing agent in the EG electrolyte enhanced the photocurrent density of the
7 CuBi₂O₄ photocathode. Adding 0.15 g of urea to the electrodeposition solution improved film
8 uniformity, enhanced PEC water splitting efficiency, and achieved a photocurrent density of -
9 1.44 mA/cm² at 0.52 V vs. RHE. This value is higher than those of previously reported CuBi₂O₄
10 photocathodes, which typically exhibit photocurrent densities below -1.0 mA/cm². To
11 understand the factors contributing to this enhanced PEC performance, this study investigated
12 the effects of varying urea concentrations (0, 0.1, 0.15, and 0.2 g per 100 mL EG) on the
13 crystallite domain size, morphology, surface roughness, light absorption, band gap, electronic
14 band structure, and PEC performance. A mechanism was proposed to account for the long-
15 term stability based on its inadequate valence band potential and irreversible degradation
16 behaviour. This work provides insights for optimizing CuBi₂O₄ thin films to enhance their
17 stability and efficiency in PEC water splitting applications.

18

19 **Keyword:** CuBi₂O₄; Electrodeposition; PEC water splitting; Photocathode; P-type
20 semiconductor

21

1 **Introduction**

2 Photoelectrochemical (PEC) water splitting, which can directly convert solar energy to
3 hydrogen, has been identified as a critical alternative for developing a more efficient,
4 sustainable, and environmentally friendly future energy system. Efficient PEC hydrogen
5 generation relies heavily on the development of suitable photocathodes. Materials such as Si,¹
6 GaAs,¹ CuO,² Cu₂O,³ LaFeO₃,⁴ CuInS₂,⁵ CuFeO₂,⁶ Sb₂Se₃,⁷ InP,⁸ and Cu₂ZnSnS₄⁹ have been
7 explored due to their conduction band potentials being more negative than the H⁺/H₂ reduction
8 potential ($E(H^+/H_2) = 0$ V vs. RHE),^{10,11} enabling energy-efficient hydrogen evolution. Among
9 p-type semiconductors, CuBi₂O₄ has attracted significant attention as a photocathode owing to
10 its low bandgap energy (1.5-1.8 eV) and favorable band structure, which predicts photocurrent
11 density of 19-27 mA/cm² under standard solar illumination (AM 1.5G, 100 mW/cm²).^{12,13}
12 However, practical application of CuBi₂O₄ thin films is significantly hindered by their intrinsic
13 limitations such as low charge carrier transfer kinetics, rapid recombination of photogenerated
14 charge carriers, and susceptibility to photocorrosion. Achieving high-quality thin films with
15 uniform thickness, controlled morphology, and strong adhesion to substrates remain essential
16 for improving the overall performance of CuBi₂O₄ thin films.

17 Various techniques, including spin coating,^{14,15} pulsed laser deposition (PLD),^{16,17}
18 physical vapor deposition (PVD) techniques (sputtering and electron beam evaporation),¹⁸⁻²⁰
19 doctor blade coating,^{21,22} spray pyrolysis,^{23,24} chemical bath deposition,^{25,26} and
20 electrodeposition,^{27,28} have been used to fabricate CuBi₂O₄ thin films. Among these,
21 electrodeposition is particularly attractive due to its low cost, mild operating temperature, and
22 ability to produce adherent interfaces, making it highly suitable for the creation of durable thin
23 films. However, non-uniform electrodeposition can reduce film quality and photocathode
24 performance. To address these issues, various strategies have been explored, including
25 adjusting the metal-ion concentration, implementing pH control through buffering, and adding
26 organic additives during the deposition process. Nakabayashi et al. improved the uniformity of
27 CuBi₂O₄ thin films by using tartrate ions to stabilize the Cu²⁺ and Bi³⁺ in solution. This
28 stabilization enabled controlled co-deposition of CuO and Bi₂O₃ at a high anodic potential.²⁹
29 After annealing at 500 °C, the resulting CuBi₂O₄ thin films exhibited enhanced coverage,
30 stronger adhesion, and better uniformity. Similarly, Hahn et al. prepared Cu-Bi
31 electrodeposition baths by dissolving Bi³⁺ and Cu²⁺ in 10% nitric acid. This step was essential
32 for fully dissolving bismuth nitrate and producing a homogeneous electrolyte, which is critical
33 for consistent electrodeposition.²⁷ The homogeneous bath enabled effective cathodic co-
34 deposition and subsequent annealing yield well-crystallized CuBi₂O₄ thin films. Citric acid has



1 also been employed as a complexing agent in CuBi₂O₄ synthesis. By forming stable metal-
2 ligand complexes, it regulates the release of metal ions during electrodeposition, thereby
3 promoting uniform film growth.³⁰

4 Urea is a small, inexpensive, and environmentally friendly molecule with strong
5 hydrogen-bonding and coordination abilities.³¹⁻³³ Its -NH₂ group can donate hydrogen bonds
6 while its carbonyl oxygen can accept them, enabling interactions with solvent molecules and
7 metal ions.³¹⁻³³ These interactions tune the solvation environment, improve ion dissolution, and
8 influence key solution properties such as ionic conductivity and viscosity, ultimately promoting
9 uniform metal deposition and controlled thin-film growth.^{31,34,35} Motivated by these
10 advantages, this work investigates the effect of urea at varying concentrations (0, 0.1, 0.15, and
11 0.2 g per 100 mL of ethylene glycol, EG) on the synthesis of CuBi₂O₄ thin film on FTO glass.
12 The resulting thin films are systematically characterized in terms of crystallite size,
13 morphology features, surface roughness, electronic band structures, and the PEC performance.
14 Based on the observed enhancements, a potential mechanism involving charge separation and
15 transfer is proposed to account for the enhancements in PEC performance.

16

17 **Experimental Procedures**

18 **Materials and chemicals**

19 The following chemicals were purchased and utilised without additional purification: Bismuth
20 (III) nitrate pentahydrate (Bi(NO₃)₃·5H₂O, 98%, Thermo Scientific Chemicals), Copper (II)
21 chloride dihydrate (CuCl₂·2H₂O, 99+, ACS reagent, Thermo Scientific Chemicals), Sodium
22 hydroxide (NaOH, 98%, extra pure, pellets, Acros Organics), and urea (CH₄N₂O, ultra-pure
23 UPS grade, Melford). Ethylene glycol (EG, C₂H₆O₂, 99%, Thermo Scientific Chemicals) was
24 used as the electrolyte for electrodeposition.

25 **CuBi₂O₄ thin film preparation**

26 A standard three-electrode system, consisting of a Pt counter electrode, an FTO working
27 electrode, and an Ag/AgCl (4 M KCl) reference electrode, was used for the electrodeposition
28 process. The FTO glass was electrically connected by placing copper tape on its edge with
29 copper tape to ensure uniform current distribution when clipped with the Autolab tweezer
30 during electrodeposition. A 100 mL EG solution comprising 6 mM Bi (NO₃)₃·5H₂O, 3 mM
31 CuCl₂, and various amounts (0 g, 0.1 g, 0.15 g, and 0.2 g) of urea was utilised as the plating
32 solution to create the Cu/Bi bimetallic films. The material was deposited by passing -0.06 C
33 per cycle at a fixed potential of E = -1.8 V versus Ag/AgCl.¹⁰ After six rounds of this cycle by



1 accumulating a total charge of -0.36 C, the resulting Cu/Bi films were heated for 2 h at 550 °C
2 in air with a ramping rate of 5 °C/min to produce the CuBi₂O₄ thin films. The samples were
3 labelled as 0.1 g-urea-6C-9mM, 0.15 g-urea-6C-9mM and 0.2 g-urea-6C-9mM, respectively.
4 As a reference, a sample generated using the same process but without adding urea into the EG
5 electrolyte was labelled as 0 g-urea-6C-9mM.

6

7 **PEC measurements**

8 The Metrohm Autolab (PGSTAT302N) electrochemical workstation with a three-electrode
9 compartment was used for all PEC analyses of the thin films. Platinum served as the counter
10 electrode, Ag/AgCl (4 M KCl) as the reference electrode, and thin film as the working electrode,
11 with 0.1 M NaOH at a pH of 12.8 as the electrolyte. A Newport 66902, 300 W xenon lamp
12 with an air mass (AM) of 1.5 was used to approximate a light intensity of 100 mW/cm² (1 sun
13 condition). The photocurrent density vs. $E_{\text{Ag/AgCl}}$ curves (J - V plots) were obtained by using
14 the linear sweeping voltammetry (LSV) mode at a constant scan rate of 10 mV/s from -0.50 to
15 0.2 V vs Ag/AgCl. At a bias potential of -0.45 V vs Ag/AgCl, the electrochemical impedance
16 spectroscopy (EIS) curves were recorded with a frequency range of 100 kHz to 0.1 Hz under a
17 modulation amplitude of 10 mV. To compare with literature results, the experimental potential
18 measured versus the Ag/AgCl reference electrode ($E_{\text{Ag/AgCl}}$) was converted to the potential
19 versus the reversible hydrogen electrode (E_{RHE}) via the following Nernst Eqn (1),^{36,37}

$$20 E_{\text{RHE}} = E_{\text{Ag/AgCl}} + E_{\text{Ag/AgCl}}^0 + 0.0591 \text{ V} \times \text{pH} \quad (E_{\text{Ag/AgCl}}^0 = 0.1976 \text{ V vs NHE at } 25 \text{ }^{\circ}\text{C}) \quad (1)$$

21 where NHE is the normal hydrogen electrode.

22

23 **Characterizations**

24 A monochromatic Cu-K α ($\lambda = 0.154$ nm) X-ray diffractometer in conjunction with a Bruker D8
25 Advance X-ray diffractometer (XRD) was used to identify the crystal structures and phases of
26 the thin films. The high-resolution surface morphology was investigated utilizing an FEI Nova
27 600 Nanolab focused ion beam-scanning electron microscope (FIB-SEM). A Bruker Innova
28 Atomic Force Microscope (AFM, USA) was also used to assess the surface morphology and
29 roughness of the thin films in a chosen region of $10 \times 10 \mu\text{m}^2$, using RTESP-300 high quality
30 etched silicon probes in a peak force tapping mode. The Nasoscope Analysis v1.7 software
31 (Bruker, USA) was applied to analyse the acquired AFM images. A Thermo Fisher Scientific



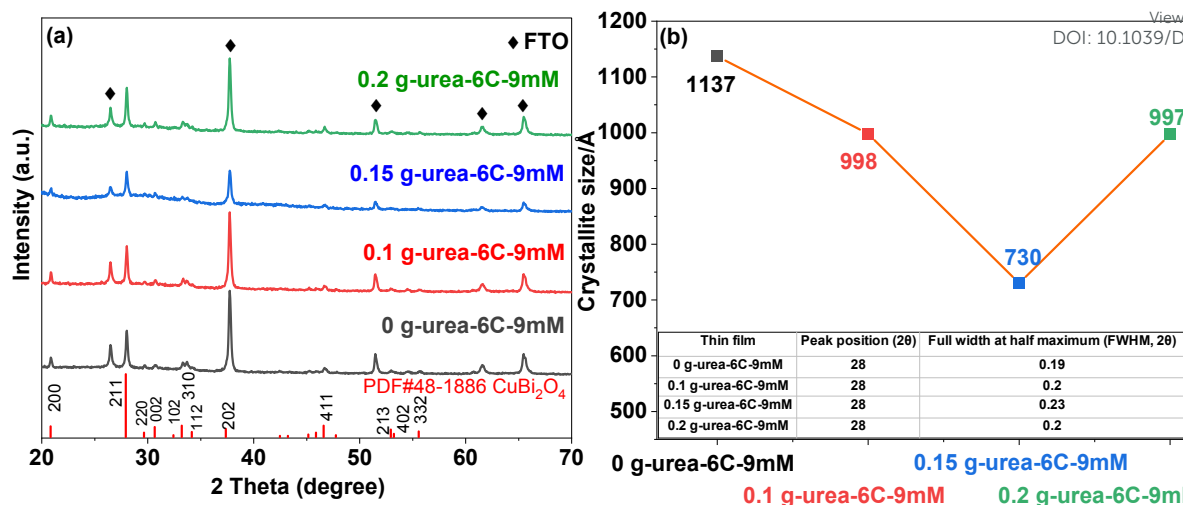
1 NEXSA spectrometer, equipped with a micro-focused monochromatic Al X-ray source (1486.7
2 eV) with an X-ray spot size of $400 \times 200 \mu\text{m}$, was used to perform the x-ray photoelectron
3 spectroscopy (XPS) and Ultraviolet photoelectron spectroscopy (UPS) analysis. The
4 photoelectron energy shift was calibrated using the C 1s electron at 284.8 eV as the reference
5 point. A PerkinElmer UV-VIS-NIR lambda 1050 spectrophotometer was used to obtain the
6 UV-visible Diffuse Reflectance Spectra (DRS) of the thin films, and the Kubelka-Munk
7 function was used to estimate the bandgap energy associated with each spectrum.

8

9 Results and Discussion

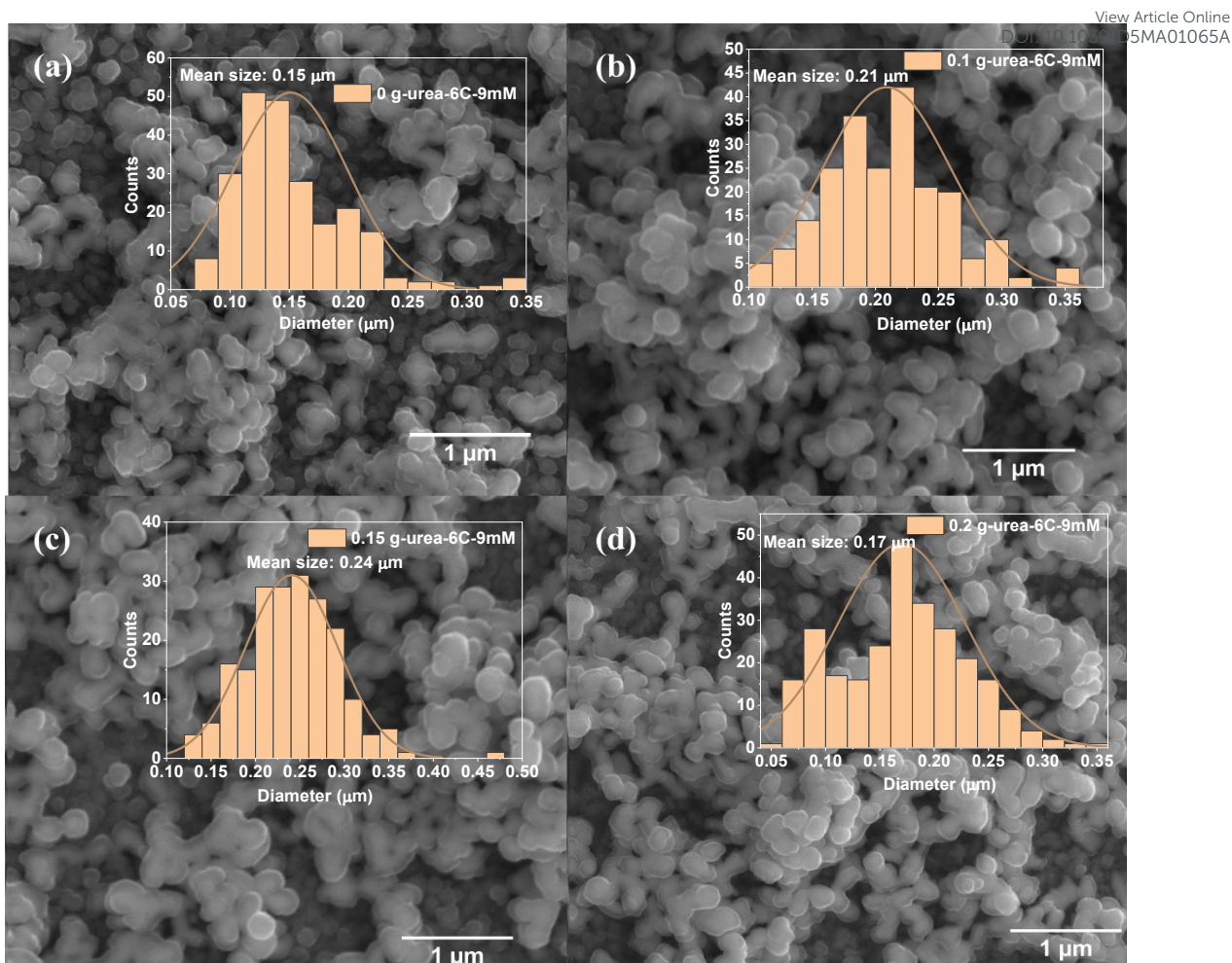
10 The XRD patterns in **Fig. 1a** showed that the thin films—0 g-urea-6C-9mM, 0.1 g-urea-6C-
11 9mM, 0.15 g-urea-6C-9mM and 0.2 g-urea-6C-9mM—exhibited similar diffraction features.
12 Specifically, the peaks at 20 degree of 20.8° , 27.9° , 29.6° , 30.6° , 32.4° , 33.2° , 34.1° , 37.4° ,
13 46.6° , 52.9° , 53.3° and 55.6° are attributed to the (200), (211), (220), (002), (102), (310), (112),
14 (202), (411), (213), (402), and (332) planes of tetragonal CuBi_2O_4 (PDF#48-1886).^{38,39} In
15 addition, five other peaks at 26.5° , 37.7° , 51.4° , 61.6° , and 65.5° are observed and ascribed to
16 the underlying FTO substrate.⁴⁰ No additional peaks or noticeable shifts were detected upon
17 the usage of the urea, indicating high phase purity of the CuBi_2O_4 thin films.

18 The crystallite size of the CuBi_2O_4 thin films was estimated based on the (211) facets
19 using the Scherrer equation,⁴¹ as presented in **Fig. 1b**, being 1137, 998, 730, and 997 Å for 0
20 g-urea-6C-9mM, 0.1 g-urea-6C-9mM, 0.15 g-urea-6C-9mM, and 0.2 g-urea-6C-9mM,
21 respectively. The variation in crystallite size can be attributed to the supersaturation-controlled
22 nucleation and growth kinetics.^{42,43} Although all samples contain identical Bi^{3+} and Cu^{2+} in 100
23 mL EG, the effective instantaneous supersaturation at the electrode is modulated by urea
24 content.^{42,43} Urea coordinates with $\text{Cu}^{2+}/\text{Bi}^{3+}$ and interacts with the solvent through hydrogen
25 bonding, controlling the rate of ion release during electrodeposition.^{31,32} With 0.15 g urea, this
26 produces a sustained supersaturation, promoting high nucleation density and restricting
27 individual crystallite growth, resulting in the smallest crystallite size (730 Å).^{42,43} Without urea,
28 rapid ion release generates a brief supersaturation spike; although the nucleation barrier is low
29 during the spike, its short duration limits the number of nuclei, leading to large crystallites
30 (1137 Å).^{42,43} At higher urea content (0.2 g), increased viscosity and slower ion diffusion again
31 reduce nucleation, allowing the crystallite to grow larger (997 Å).^{42,43}



2 **Fig. 1** (a) XRD patterns and (b) corresponding crystallite size of different CuBi₂O₄ thin films
3 deposited on FTO substrate.

5 The surface morphologies of the CuBi₂O₄ thin films were examined by SEM, with
6 representative low-magnification images shown in **Fig. S3** and high-magnification images in
7 **Fig. 2**. All CuBi₂O₄ thin films exhibit uneven and rough surface features, with some regions
8 containing small nanoparticles, while in others the nanoparticles coalesce into larger branched
9 structures, forming interconnected networks. These networks display irregular, coral-like
10 morphologies reminiscent of finger coral, characterized by pronounced variations in particle
11 size, spatial distribution, and height. The size differences of nanoparticles among the four
12 CuBi₂O₄ thin films were estimated from the particle diameter distribution histograms shown in
13 **Fig. 2**. Specifically, the average diameter of sample without urea (0 g-urea-6C-9mM) is 0.15
14 μm, whilst being 0.21 and 0.17 μm, respectively, for 0.1 g-urea-6C-9mM and 0.2 g-urea-6C-
15 9mM, being the largest average diameter of 0.24 μm for sample 0.15 g-urea-6C-9mM. This
16 behavior can be understood by combining classical nucleation and growth with non-classical
17 aggregation mechanisms:^{42,43} small crystallites with high surface energy tend to aggregate,
18 forming larger particles. With 0.15 g urea, moderated ion release sustains supersaturation,
19 generating many small crystallites that aggregate in a controlled manner, producing well-
20 packed particles and uniform films. Without or with excess urea, nucleation is limited and
21 aggregation is slowed, resulting in less uniform particles. The low-resolution SEM images in
22 **Fig. S3** further highlight the differences in coral-like interconnected networks distribution, with
23 the urea-containing thin films, especially 0.1 g-urea-6C-9mM and 0.15 g-urea-6C-9mM thin
24 films, showing the most pronounced branched structures.

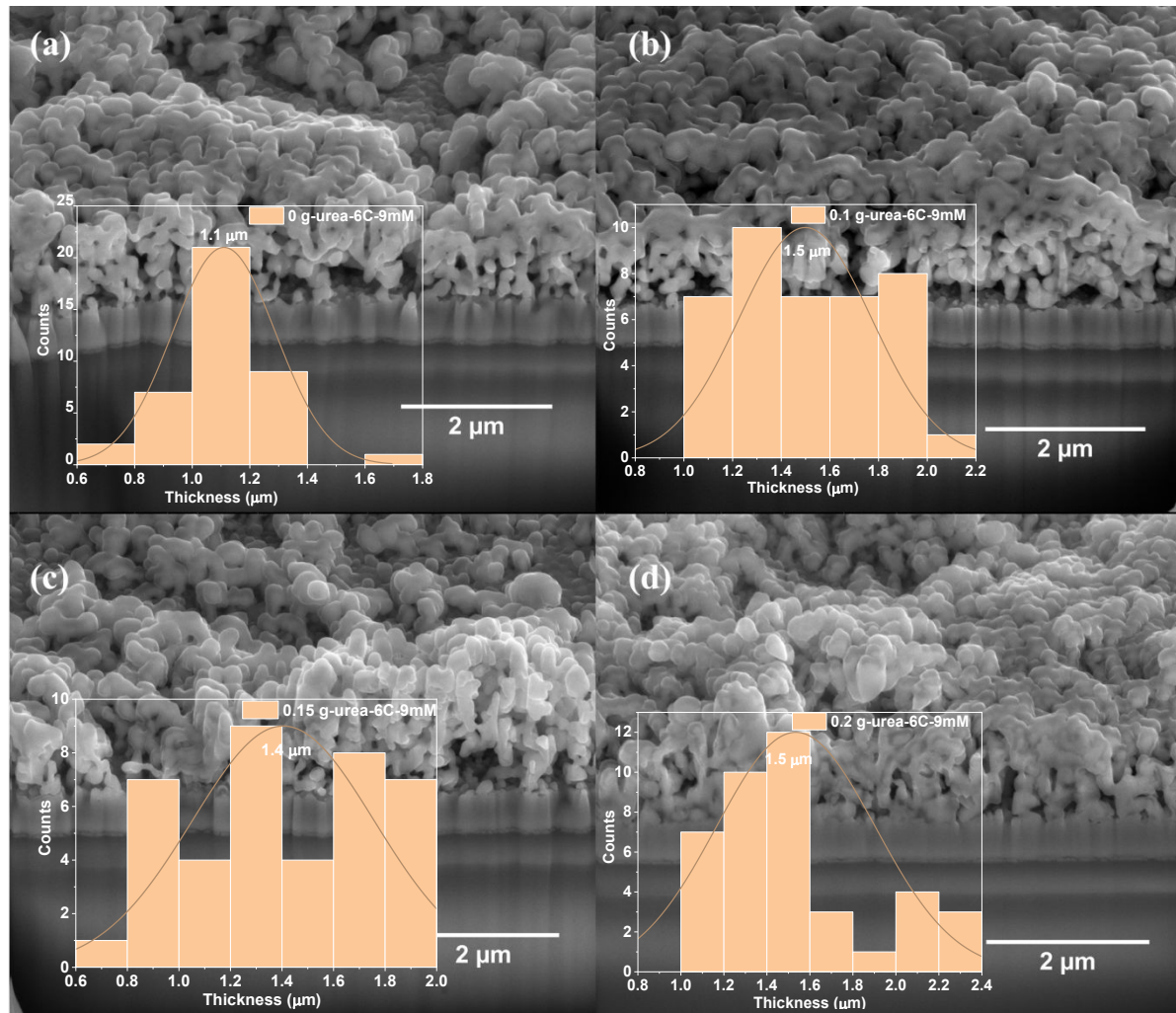


1 **Fig. 2** SEM images of the top view and particle size distribution histograms of the resulting
 2 CuBi₂O₄ thin films on FTO substrates: (a) 0 g-urea-6C-9mM; (b) 0.1 g-urea-6C-9mM; (c) 0.15
 3 g-urea-6C-9mM; and (d) 0.2 g-urea-6C-9mM.

4
 5 The cross-sectional SEM images in **Fig. 3** reveal that all CuBi₂O₄ thin films are composed of
 6 nanoparticle aggregates coalesced into porous, irregular networks. Their vertical height of these
 7 branched regions varies, and the mean thickness were determined from the thickness histogram
 8 in **Fig. 3**. The thin film prepared under urea-free conditions (0 g-urea-6C-9mM) exhibits a
 9 moderately compact structure with a mean thickness of ~1.1 μm. In contrast, films deposited
 10 from urea-containing electrolytes display increased thicknesses of ~1.5 μm (0.1 g-urea-6C-
 11 9mM), ~1.4 μm (0.15 g-urea-6C-9mM), and ~1.5 μm (0.2 g-urea-6C-9mM). These results
 12 show that urea promotes vertical growth by moderating ion release during electrodeposition,
 13 which enhances nucleation and aggregation along the vertical direction, leading to thicker,
 14 more pronounced branched structures. EDS spectra displayed in **Fig. S4** show that Cu, Bi, O,
 15 Sn, Si, and the coated C are present in all thin films. The Cu/Bi atomic ratios of all samples,
 16 derived from EDS analysis, are 3.09: 6.39 for 0 g-urea-6C-9mM, 3.49: 7.62 for 0.1 g-urea-6C-



1 9mM, 9.86: 19.48 for 0.15 g-urea-6C-9mM, and 0.97: 1.94 for 0.2 g-urea-6C-9mM. These values
 2 correspond closely to a Cu: Bi ratio of approximately 1: 2, consistent with the stoichiometric
 3 composition of CuBi_2O_4 . This result demonstrates the successful synthesis of CuBi_2O_4 thin
 4 films, which is consistent with the XRD analysis.

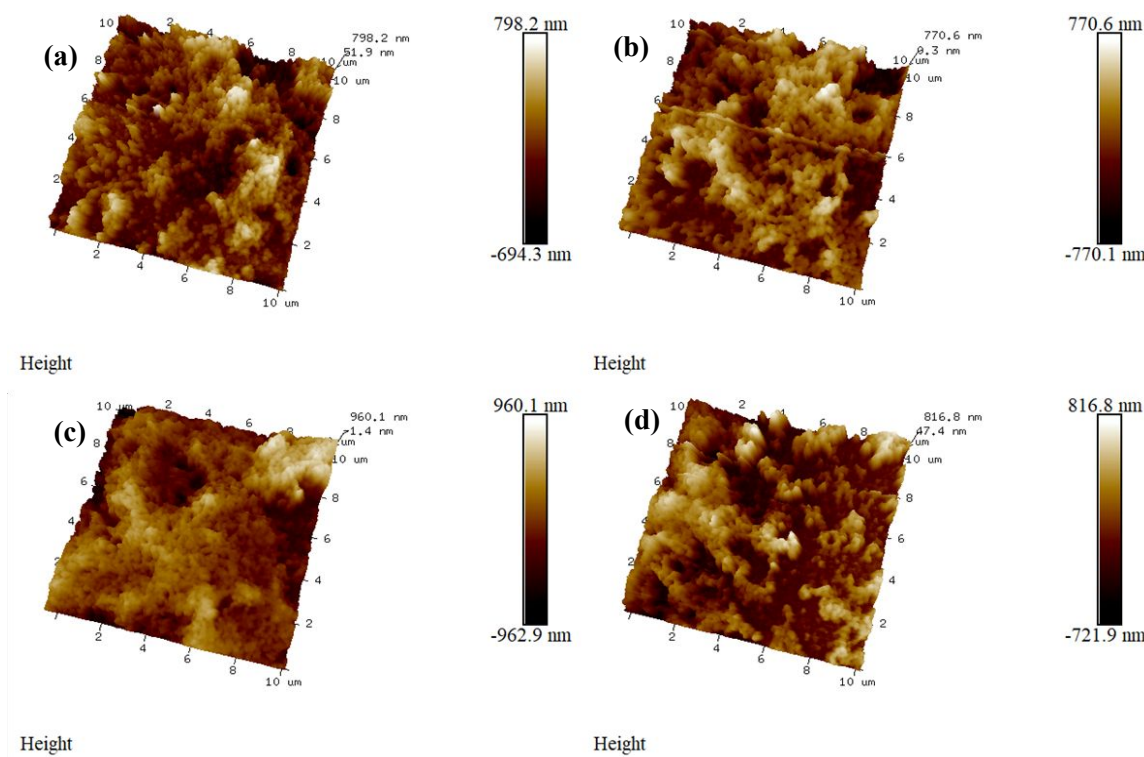


5 **Fig. 3** SEM images of Cross-section views and thickness histograms of the resulting CuBi_2O_4
 6 thin films on FTO substrates: (a) 0 g-urea-6C-9mM; (b) 0.1 g-urea-6C-9mM; (c) 0.15 g-urea-
 7 6C-9mM; and (d) 0.2 g-urea-6C-9mM.

8
 9 Three-dimensional (3D) perspective topographical pictures displayed in **Fig. 4** present the
 10 vertical height variations caused by the bumps, pits, or other surface irregularities. The
 11 topologies of all the CuBi_2O_4 thin films demonstrate a non-uniform growth, characterized by
 12 areas where certain regions grow aggressively into large and high-height features, while other
 13 parts exhibit minimal growth. Specifically, thin films of 0.1 g-urea-6C-9mM and 0.15 g-urea-
 14 6C-9mM show more uniform distributions of large, high-height regions compared with thin
 15 films 0 g-urea-6C-9mM and 0.2 g-urea-6C-9mM. The two-dimensional (2D) views, showing

1 the height signals along the given section lines, the corresponding mean roughness (R_a) the
 2 maximum height (R_{max}) values, and other related parameters, are presented in **Fig. S5**. Where
 3 R_{max} is defined as the height difference between the highest and lowest points on the cross-
 4 sectional profile relative to the centre line over the length of the profile. The variations in the
 5 R_{max} values indicate the non-uniform topology features of the thin films. The surface average
 6 R_a values of the CuBi_2O_4 thin films are 181.1 nm for sample 0 g-urea-6C-9mM, 174.9 nm for
 7 sample 0.1 g-urea-6C-9mM, sample 0.15 g-urea-6C-9mM for 154.2 nm, and 185.1 nm for 0.2
 8 g-urea-6C-9mM (**Fig. S5**), indicating a more uniform surface for samples 0.1 g-urea-6C-9mM
 9 and 0.15 g-urea-6C-9mM.

10



11 **Fig. 4** AFM 3D perspectives of (a) 0 g-urea-6C-9mM, (b) 0.1 g-urea-6C-9mM, (c) 0.15 g-urea-
 12 6C-9mM, and (d) 0.2 g-urea-6C-9mM.

13

14 According to the XPS survey scan results shown in **Fig. S6**, both samples have similar
 15 entire spectra with Cu 2p, Bi 4f, and O 1s peaks. **Fig. 5a** reveals the high-resolution Bi 4f
 16 spectra of samples 0 g-urea-6C-9mM and 0.15 g-urea-6C-9mM. The binding energies at 158.6
 17 and 163.9 eV are responsible for the typical spin-orbit split Bi 4f_{7/2} and Bi 4f_{5/2} peaks,
 18 respectively, which are brought on by the Bi³⁺ component in both samples.^{44,45} The small peaks
 19 fitted at lower binding energies of 162.2 and 156.9 eV are attributed to residual metallic Bi on

1 the surface of the CuBi₂O₄ lattice.^{46,47} In **Fig. 5b**, the raw data exhibit four peaks: a doublet for
2 Cu 2p and two additional shake-up peaks. These shake-up peaks are attributed to a strong
3 interaction of the final states, involving charge transfer from O 2p band to the Cu 3d band.^{48,49}
4 Cu 2p spectra are typically featured by focusing on the Cu 2p_{3/2} peak and the lower binding
5 energy shake-up peak, owing to their distinctive spectral features that allow for reliable fitting.
6 Peaks with binding energies of 933.9 and 932.3 eV, fitted from the Cu 2p_{3/2} peak, are attributed
7 to the Cu²⁺ in the CuBi₂O₄ lattice and Cu⁺ species, respectively.^{44,49} Peaks located at 943.7 and
8 941.2 eV, obtained from the lower binding energy shake-up peak, further suggest the
9 coexistence of these Cu²⁺ and Cu⁺ species within the CuBi₂O₄ thin films. The peak area ratios
10 of Bi³⁺ and Bi (9: 1), as well as that of Cu²⁺ and Cu⁺ (8: 2), in the 0.15 g-urea-6C-9mM thin
11 film and 0 g-urea-6C-9mM thin film, are maintained without significant change. This indicates
12 that the addition of urea into the electrolyte during the electrodeposition process does not
13 significantly affect the chemical composition and the chemical states of the CuBi₂O₄ thin film.
14 To further confirm the chemical states and quantify the surface concentration of Cu species in
15 the CuBi₂O₄ thin film, the Cu LM2 Auger spectra were analysed. As depicted in **Fig. 5c**, the
16 Cu LM2 Auger electron spectra show peaks corresponding to the lattice Cu²⁺ (blue peaks) and
17 the low-valence Cu⁺ species (red peaks).^{50,51} This finding is consistent with the results obtained
18 from the Cu 2p spectra. The O 1s spectra (**Fig. 5d**) for both CuBi₂O₄ samples were fitted into
19 three distinct peaks at binding energies of approximately 529.4, 530.5, and 531.4 eV. These
20 peaks are attributed to lattice oxygen (O_L),⁵⁰⁻⁵² surface hydroxyl group,^{50,51} and absorbed water
21 species, respectively. The presence of surface hydroxyl groups in CuBi₂O₄ is commonly
22 associated with surface oxygen environments influenced by the coexistence of Cu<sup>2+}/Cu⁺ states,
23 as observed in the Cu LM2 Auger spectra. The O_L peak area ratios for CuBi₂O₄ thin films of 0
24 g-urea-6C-9mM and 0.15 g-urea-6C-9mM are 49.5 % and 47.2%, respectively, while the
25 surface hydroxyl species for these two CuBi₂O₄ thin films are 39.3% and 42.1%, respectively.
26 This variation may be attributed to the different distribution of aggregated, finger coral-like
27 structures on the surface of the thin films.</sup>



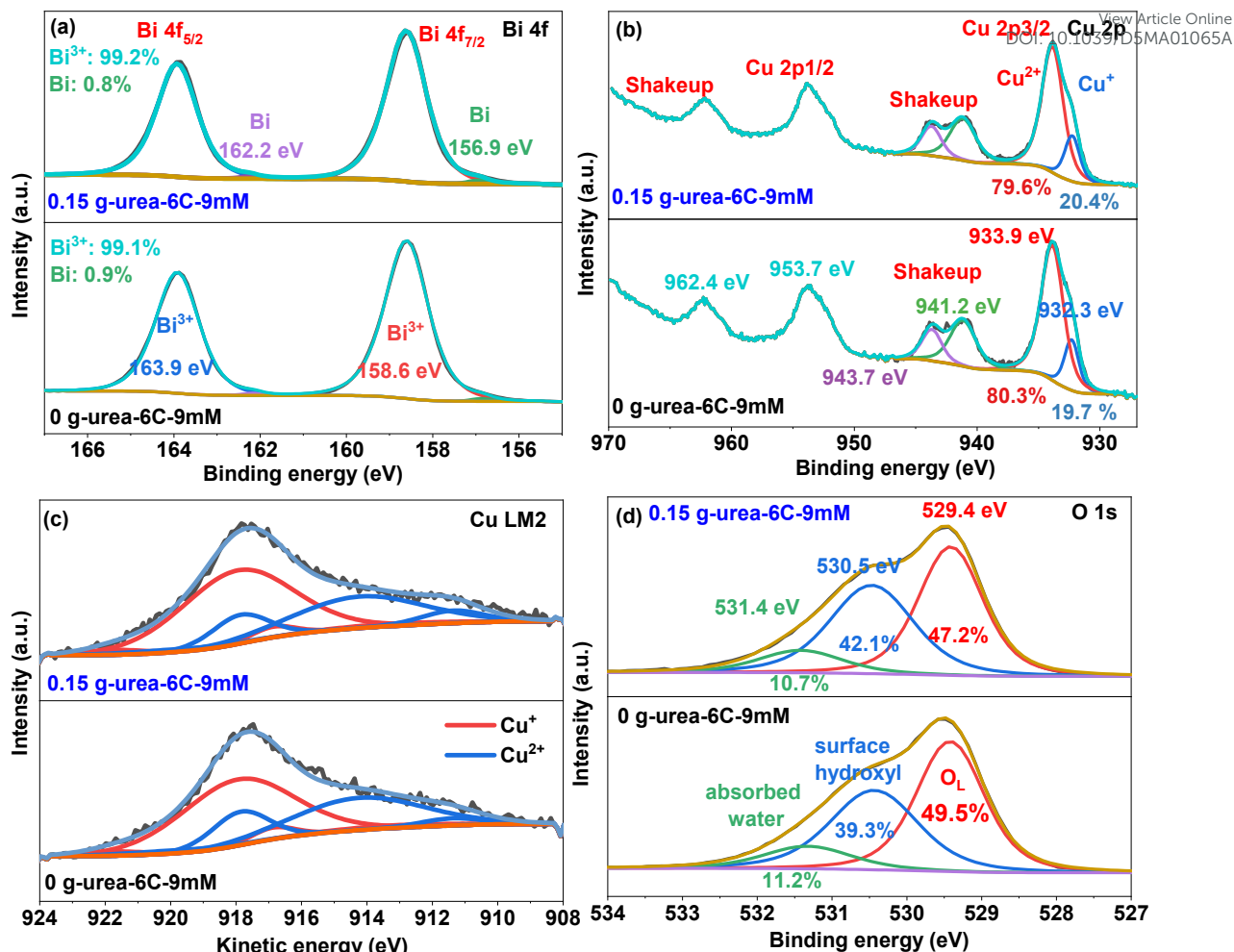
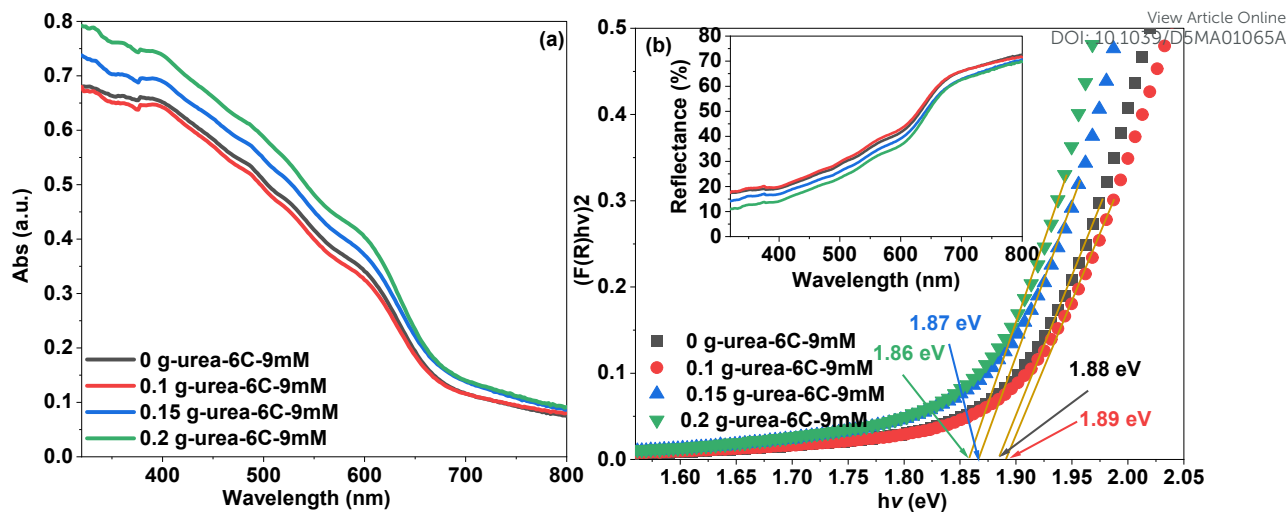


Fig. 5 XPS spectra of prepared CuBi₂O₄ thin films: 0 g-urea-6C-9mM and 0.15 g-urea-6C-9mM. (a) Bi 4f, (b) Cu 2p, (c) Cu LM2, and (d) O 1s.

The UV-visible absorbance spectra (**Fig. 6a**) exhibit strong visible-light absorptions in all thin films. The incident light absorbances of the CuBi₂O₄ thin films: 0.15 g-urea-6C-9mM and 0.2 g-urea-6C-9mM are higher compared with those of 0 g-urea-6C-9mM and 0.1 g-urea-6C-9mM CuBi₂O₄. Slight red shifts can be observed upon introducing 0.15 g and 0.2 g urea into the electrodeposition process. This increase in optical absorption and reduction in reflectance (**Fig. 6b**, inset) are attributed to the varying surface topographical features induced by the urea. **Fig. 6b** presents the direct transition band gap values for the samples—1.88 eV for sample 0 g-urea-6C-9mM, 1.89 eV for sample 0.1 g-urea-6C-9mM, 1.87 eV for sample 0.15 g-urea-6C-9mM, and 1.86 eV for sample 0.2 g-urea-6C-9mM. These values are consistent with those reported in previous studies.¹³





1 **Fig. 6** (a) UV-visible absorbance spectra of the CuBi₂O₄ thin films and (b) the corresponding
2 predicted band gap values from the Kubelka-Munk function,⁵³ with the UV-visible Diffuse
3 Reflectance Spectra (DRS) shown inset.
4

5
6 Mott-Schottky measurements are utilized at 1 kHz in 0.1 M NaOH solution in dark
7 condition, to estimate the flat band potential (E_{fb}) and the hole density (N_A) of the CuBi₂O₄
8 thin films. The Mott-Schottky plots depicted in **Fig. 7a** were obtained from the following Eqn
9 (2):⁵⁴

$$10 \quad \frac{1}{C^2} = \frac{2}{A^2 e \epsilon \epsilon_0 N_A} \left(-E + E_{fb} - \frac{KT}{e} \right) \quad (2)$$

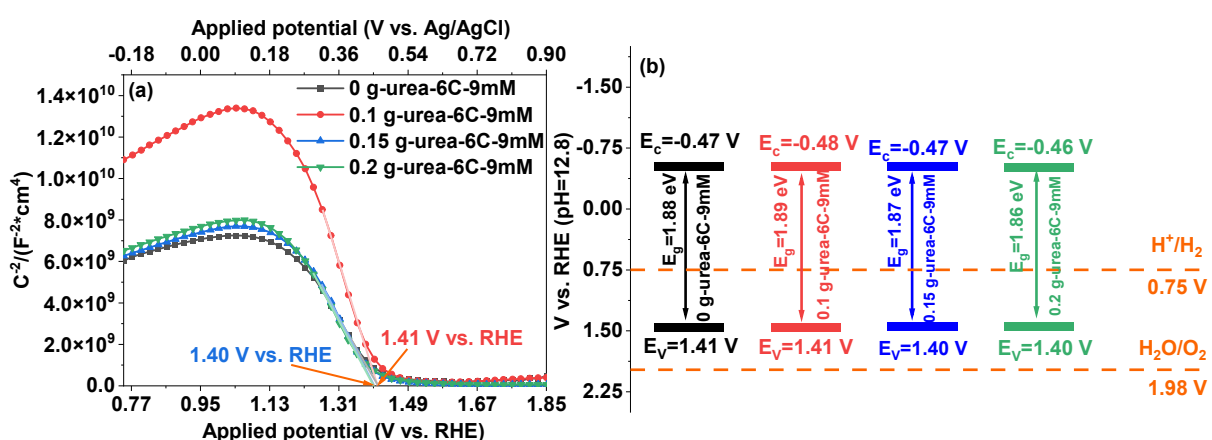
11 where the parameters C, A, E_{fb} , N_A , ϵ , ϵ_0 , and E correspond to the capacitance, the electrode
12 surface area (1×10^{-4} m²), the flat-band potential, the acceptor density, the relative
13 permittivity (dielectric constant) of 80 as reported previously,^{54,55} the permittivity of free space
14 (8.854×10^{-12} F/m),³⁶ and the applied potential, respectively.⁵⁴ As shown in **Fig. 7a**, the
15 corresponding values of the slope and hole densities of the CuBi₂O₄ thin films were calculated
16 and listed in **Table 1**.¹² All the regression lines exhibit negative slopes, indicating that the
17 samples are p-type semiconductor.³⁸ Comparison of the N_A values indicates that all samples
18 exhibit hole densities of the same order of magnitude. Sample 0 g-urea-6C-9mM shows the
19 highest hole density, likely due to the transition from Cu⁺ to Cu²⁺, which releases electrons and
20 thereby enhances the hole density. The flat band potentials of the CuBi₂O₄ thin films are 1.41
21 V vs. RHE for samples 0 g-urea-6C-9mM and 0.1 g-urea-6C-9mM, and 1.40 V vs. RHE for
22 sample 0.15 g-urea-6C-9mM and sample 0.2 g-urea-6C-9mM, respectively. In p-type

1 semiconductors, the flat band potential is approximately aligned with the energy level near the
 2 valence band edge.⁵⁶ The potential of the conduction band can be determined based on the
 3 following Eqn (3).⁵⁷

4 $E_c = E_v - E_g$ (3)

5 The potentials of both the conduction and valence band positions relative to the water redox
 6 potential were constructed and illustrated in **Fig. 7b**. The valence band potentials of all the thin
 7 films at pH 12.8 are above 1.98 V vs. RHE (corresponding to 1.23 V vs. RHE at pH 0), while
 8 the conduction band potentials are above 0.75 V vs. RHE (corresponding to 0 V vs. RHE at pH
 9 0).⁵⁸ Therefore, the CuBi₂O₄ thin films demonstrate the capability to perform the hydrogen
 10 evolution reaction under a pH of 12.8. Additionally, the band edge positions differ by only 10
 11 mV, which is within the range of experimental error and would not significantly affect the
 12 overall band structure. The ultraviolet photoelectron spectroscopic (UPS) analysis using a He
 13 (I) laser ($h\nu = 21.22$ eV) as the incident light was utilized to determine the work functions of
 14 the CuBi₂O₄ thin films. As illustrated in **Fig. S7**, the work functions for samples 0 g-urea-6C-
 15 9mM and 0.15 g-urea-6C-9mM are 5.03 eV and 5.21 eV, respectively. Therefore, the energy
 16 required to extract electrons from the materials differs by a maximum of 0.2 eV, which is quite
 17 similar and might not be enough to affect the PEC water splitting performance.

18



19 **Fig. 7** Mott-Schottky plots (a) and (b) the estimated band structures of the CuBi₂O₄ thin films.

21

22

1 **Table 1** Band edge potential position, Mott-Schottky slope value, and corresponding **hole**
 2 densities.

Thin film	Conduction band potential (V vs. RHE)	Valence band potential (V vs. RHE)	the value of the slope	N_A (cm ⁻³)
0 g-urea-6C-9mM	-0.47	1.41	-3.18E10	5.54E19
0.1 g-urea-6C-9mM	-0.48	1.41	-5.94E10	2.97E19
0.15 g-urea-6C-9mM	-0.47	1.40	-3.57E10	4.94E19
0.2 g-urea-6C-9mM	-0.46	1.40	-3.46E10	5.09E19

3

4 The $J-V$ and Nyquist plots are displayed in **Fig. 8**, which were obtained from linear
 5 sweeping voltammetry (LSV) and frequency response analyser (FRA) impedance
 6 potentiostatic mode, respectively, for the investigation of the PEC performance of the CuBi₂O₄
 7 thin films. In **Fig. 8a**, sample 0 g-urea-6C-9mM exhibits the highest photocurrent density of -
 8 0.94 mA/cm² at 0.52 V vs. RHE, whilst the photocurrent density was further improved after
 9 the introduction of urea during the electrodeposition process, reaching -1.04 and -1.44 mA/cm²
 10 for the 0.1 and 0.15 g urea samples, which is higher than previously published values (**Table**
 11 **S2**). Further increasing the amount of urea to 0.2 g led to a decreased photocurrent density of -
 12 0.99 mA/cm², which is still greater than that of sample 0 g-urea-6C-9mM. Therefore, the
 13 charge separation and transfer efficiencies have been improved. The Nyquist spectra (**Fig. 8b**)
 14 fitted via the following equivalent circuit inserted in the **Fig. 8b** are applied to investigate the
 15 charge-transfer resistance of the CuBi₂O₄ thin films. R_s represents the intercept of the
 16 semicircle with the real axis (Re(Z)) at low frequency, indicating the resistance of the
 17 electrolyte solution and any inherent resistance of the setup. The diameter of the semicircle in
 18 the Nyquist plot is utilized to determine the charge transfer resistance (R_{ct}) at the interface of
 19 the CuBi₂O₄ thin film and FTO glass. The double-layer capacitance (C_{dl}) represents the
 20 capacitive behaviour at the interface, while the Warburg impedance (W) indicates the influence
 21 of the diffusion processes on the impedance response in combination with the double-layer
 22 capacitance. According to **Fig. 8b** and **Table 2**, sample 0.15 g-urea-6C-9mM, which exhibits
 23 the smallest semicircle diameter, has the lowest charge transfer resistances (R_{ct}) with a value



View Article Online
DOI: 10.1039/DMA01065A

of $2430\ \Omega$. This is followed by sample 0.2 g-urea-6C-9mM ($R_{ct} = 3193\ \Omega$), and sample 0.1 g-urea-6C-9mM ($R_{ct} = 4169\ \Omega$), whilst the urea-free reference CuBi_2O_4 thin film exhibits the highest charge transfer resistance of $5441\ \Omega$. Therefore, the charge transfer efficiencies of the CuBi_2O_4 thin films are ranked as follows: 0.15 g-urea-6C-9mM > 0.2 g-urea-6C-9mM > 0.1 g-urea-6C-9mM > 0 g-urea-6C-9mM under the bias of 0.52 V vs. RHE. The C_{dl} values, however, exhibit an opposite trend, with the 0.15 g-urea-6C-9mM thin film showing the highest C_{dl} value. This implies a larger area for charge separation, potentially enhancing the PEC performance. The observed decrease in charge transfer resistance, coupled with the increased C_{dl} , indicates an improved efficiency in utilizing photogenerated charges for these thin films.

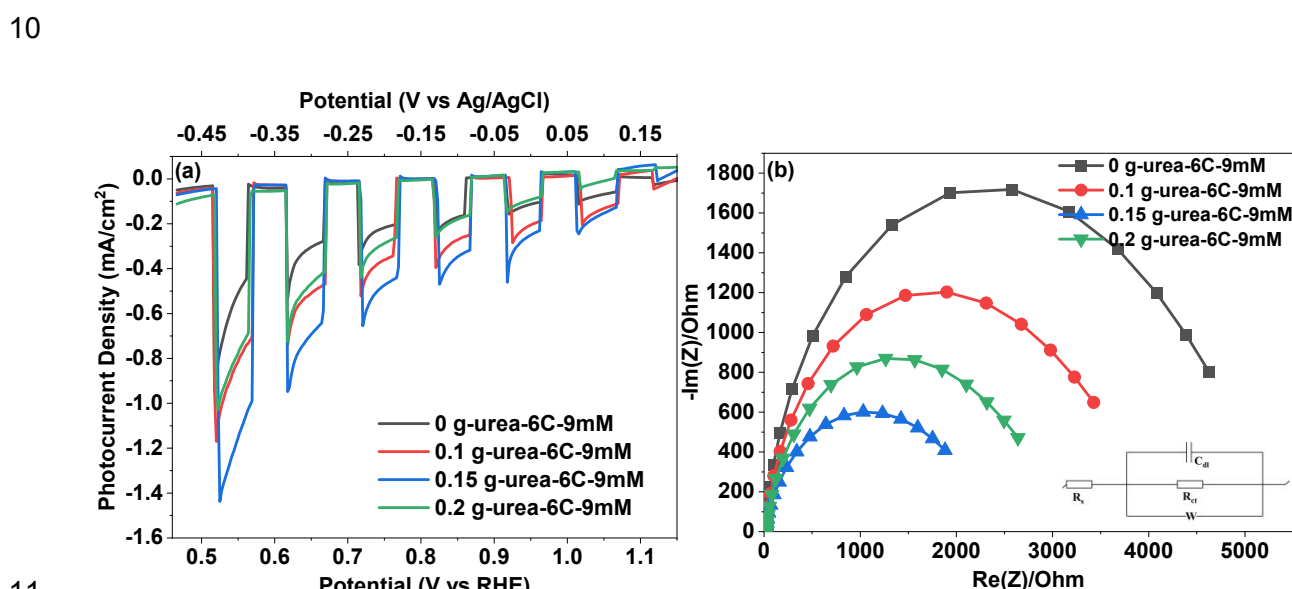


Fig. 8 (a) Photocurrent density-potential vs. RHE or Ag/AgCl ($J-V$) plots under chopped illumination condition, (b) EIS Nyquist plots obtained at -0.45 V vs. Ag/AgCl under one sun simulated light illumination.

15

16 **Table 2** parameters: R_s , R_{ct} , C_{dl} , and W obtained from the fitted Nyquist plots of the CuBi_2O_4 thin films.

	0 g-urea-6C-9mM	0.1 g-urea-6C-9mM	0.15 g-urea-6C-9mM	0.2 g-urea-6C-9mM
R_s	$26.22\ \Omega$	$23.06\ \Omega$	$20.75\ \Omega$	$25.31\ \Omega$
R_{ct}	$5441\ \Omega$	$4169\ \Omega$	$2430\ \Omega$	$3193\ \Omega$
C_{dl}	$15.26\ \mu\text{F}$	$16.58\ \mu\text{F}$	$18.29\ \mu\text{F}$	$15.25\ \mu\text{F}$

<i>W</i>	14593 $\Omega \cdot s^{0.5}$	9099 $\Omega \cdot s^{0.5}$	3925 $\Omega \cdot s^{0.5}$	6932 $\Omega \cdot s^{0.5}$
----------	------------------------------	-----------------------------	-----------------------------	-----------------------------

1	14593 $\Omega \cdot s^{0.5}$	9099 $\Omega \cdot s^{0.5}$	3925 $\Omega \cdot s^{0.5}$	6932 $\Omega \cdot s^{0.5}$
---	------------------------------	-----------------------------	-----------------------------	-----------------------------

2 The stability of the CuBi₂O₄ thin films has been investigated using I-t curves measured
 3 through chronoamperometry under continuous solar light illumination for 2 h at 0.52 V vs.
 4 RHE. Thin film 0.15 g-urea-6C-9mM, which exhibits the highest photocurrent density, was
 5 used to investigate the stability performance in comparison to thin film 0 g-urea-6C-9mM. As
 6 shown in **Fig. S8**, both thin films showed poor PEC stabilities. Specifically, initial sharp drops
 7 in photocurrent density were observed within approximately 10 seconds. After 100 seconds of
 8 continuous illumination, both films reached their steady-state photocurrents, with sample 0.15
 9 g-urea-6C-9mM exhibiting approximately -0.27 mA/cm², which is about 42% higher than the
 10 reference (-0.19 mA/cm²).

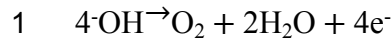
11 The variations in PEC performance (photocurrent density and photostability) of the
 12 CuBi₂O₄ thin films can be primarily attributed to the urea-induced morphological differences.
 13 Examination of the charge-time curves (**Fig. S9**) recorded during electrodeposition reveals that
 14 the presence of urea slows the deposition process under the same applied charges. This effect
 15 arises from the coordination of urea with Cu²⁺ and Bi³⁺ ions, which stabilizes them in solution
 16 and maintains a steady concentration of electroactive species.^{59,60} This behavior further
 17 supports the sustained-supersaturation condition proposed earlier, which governs both the
 18 nucleation rate and subsequent particle aggregation. Under the influence of urea, the resulting
 19 more continuous particle networks and slightly increased film thickness provide more efficient
 20 charge-transport pathways and reduce recombination at interparticle boundaries, accounting
 21 for the higher photocurrent densities of the urea-assisted thin films. Moreover, the improved
 22 structural coherence and uniformity help to moderate photocorrosion, explaining the modest
 23 enhancement in stability compared to the referent thin film (0 g-urea-6C-9mM).

24 Based on above analyses, a possible charge separation and transfer mechanism has been
 25 proposed to explain the improved PEC water splitting performance. As illustrated in **Fig. 9**,
 26 under solar light illumination, the CuBi₂O₄ thin film generates photocarriers after absorbing
 27 light with energy greater than its band gap. A built-in electric field separates the photo-
 28 generated electrons and holes. Ideally, the electrons will transfer to the surface of the CuBi₂O₄
 29 thin film to participate in the reduction reaction Eqn (4):⁶¹



31 Meanwhile, the Pt counter electrode serves as the site for the oxidation reaction Eqn (5):⁶¹

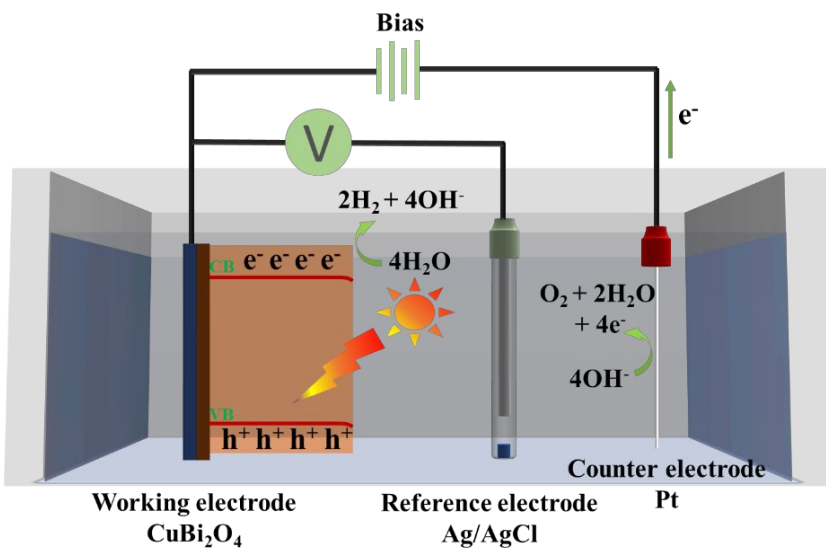




2 The generated electrons at the counter electrode flow through the external circuit back to the
 3 CuBi_2O_4 thin film, completing the electrical circuit. However, an undesirable photocorrosion
 4 reaction occurs within the CuBi_2O_4 thin film due to the insufficiently anodic valence band
 5 potential of the synthesized CuBi_2O_4 photocathode (1.4 V vs. RHE at pH 12.8). This
 6 thermodynamic limitation prevents the efficient oxygen evolution reaction (OER), leading to
 7 the photogenerated holes oxidizing the CuBi_2O_4 lattice and degrading the Cu-O-Bi framework
 8 into CuO and Bi_2O_3 rather than driving water oxidation (1.98 V vs. RHE at pH 12.8).⁶²⁻⁶⁴
 9 Furthermore, in an alkaline electrolyte, Bi^{3+} within the CuBi_2O_4 lattice reacts with hydroxide
 10 ions to form soluble hydroxo complexes,⁶² leading to the bismuth leaching effect and structural
 11 destabilization. Simultaneously, Cu^+ species undergo the following disproportionation Eqn
 12 (6):⁶³



14 where the resulting Cu^{2+} species react with hydroxide ions to form hydroxy complexes,⁶³ which
 15 further accelerates the lattice degradation. The residual photocurrent remains due to the
 16 presence of surviving CuBi_2O_4 domains and the photoactivity of the secondary phases.



17

18 **Fig. 9** Schematic illustration of the electronic transfer under the possible mechanism.

19

20

1 **Conclusions**

2 This work successfully developed a CuBi₂O₄ photocathode with an interconnected nanoparticle
3 textured morphology for PEC water splitting. AFM characterization showed that the CuBi₂O₄
4 thin film prepared with 0.15 g urea per 100 mL of EG exhibited the lowest surface roughness
5 and best uniformity compared with thin films prepared with other urea concentrations. XPS
6 analyses revealed that the element composition and chemical states, as well as the electronic
7 band structures observed through electrochemical characterization, remained largely
8 unchanged. This indicated that the variations of urea in the EG electrolyte primarily contributed
9 to the physical differences, such as crystallite size, uniformity and thickness, rather than
10 affecting the chemical performance. Durability tests demonstrated that, after 100 seconds of
11 continuous illumination, the 0.15 g-urea-6C-9mM CuBi₂O₄ thin film stabilized at
12 approximately -0.27 mA/cm², while the 0 g-urea-6C-9mM CuBi₂O₄ thin film stabilized at -
13 0.19 mA/cm². This represents a 42% enhancement in stability for the 0.15 g-urea-6C-9mM
14 CuBi₂O₄ thin film, which is attributed to its more uniform morphology. These fundings
15 underscore the introduction of urea into the EG electrolyte enhances the uniformity and
16 performance of CuBi₂O₄ thin film, thereby improving their effectiveness in PEC water splitting
17 applications.

[View Article Online](#)
DOI: 10.1039/D5MA01065A

1 **Conflict of interests**

2 The authors declare that they have no known competing financial interests or personal
3 relationships that could have appeared to influence the work reported in this paper.

4

1 Data availability

2 All data supporting the findings of this study are included within the article and its Electronic
3 Supplementary Information (ESI).

4

1 Acknowledgements

2 A. A. Tahir and Y. Zhu acknowledge the Engineering and Physical Sciences Research Council
3 (EPSRC), UK, under research grant numbers EP/T025875/1 and EP/V049046/1. The author
4 X. Yang would like to acknowledge the financial support from the University of Exeter-China
5 Scholarship Council PhD Scholarship. The authors would also like to thank Dr. Shaoliang
6 Guan of the University of Cardiff for his effort to the XPS equipment support. For the purpose
7 of open access, the authors have applied a Creative Commons Attribution (CC BY) licence to
8 any Author Accepted Manuscript version arising from this submission

[View Article Online](#)
DOI: 10.1039/D5MA01065A

1 **References**

2 1. Y. H. Lee, J. Kim and J. Oh, *ACS Appl. Mater. Interfaces*, 2018, 10, 33230-33237,
3 <https://doi.org/10.1021/acsami.8b10943>.

4 2. S. Masudy-Panah, R. S. Moakhar, C. S. Chua, A. Kushwaha, T. I. Wong and G. K. Dalapati,
5 *RSC Adv.*, 2016, 6, 29383-29390, <https://doi.org/10.1039/c6ra03383k>.

6 3. J. Luo, L. Steier, M.-K. Son, M. Schreier, M. T. Mayer and M. Grätzel, *Nano Lett.*, 2016,
7 16, 1848-1857, <https://doi.org/10.1021/acs.nanolett.5b04929>.

8 4. G. S. Pawar, A. Elikkottil, S. Seetha, K. S. Reddy, B. Pesala, A. A. Tahir and T. K. Mallick,
9 *ACS Appl. Energy Mater.*, 2018, 1, 3449-3456, <https://doi.org/10.1021/acsaelm.8b00628>.

10 5. Q. Cai, Z. Liu, C. Ma, Z. Tong and C. Han, *J. Mater. Sci.: Mater. Electron.*, 2018, 29, 20629-
11 20638, <https://doi.org/10.1007/s10854-018-0201-z>.

12 6. R.-P. Li, S.-M. Yu and Z.-Y. Zhao, *Mater. Chem. Phys.*, 2024, 311, 128582,
13 <https://doi.org/10.1016/j.matchemphys.2023.128582>.

14 7. W. Yang, S. Lee, H. C. Kwon, J. Tan, H. Lee, J. Park, Y. Oh, H. Choi and J. Moon, *ACS
15 Nano*, 2018, 12, 11088-11097, <https://doi.org/10.1021/acsnano.8b05446>.

16 8. P. R. Narangari, J. D. Butson, H. H. Tan, C. Jagadish and S. Karuturi, *Nano Lett.*, 2021, 21,
17 6967-6974, <https://doi.org/10.1021/acs.nanolett.1c02205>.

18 9. N. Guijarro, M. S. Prevot and K. Sivula, *J. Phys. Chem. Lett.*, 2014, 5, 3902-3908,
19 <https://doi.org/10.1021/jz501996s>.

20 10. D. Kang, J. C. Hill, Y. Park and K.-S. Choi, *Chem. Mater.*, 2016, 28, 4331-4340,
21 <https://doi.org/10.1021/acs.chemmater.6b01294>.

22 11. S. P. Berglund, F. F. Abdi, P. Bogdanoff, A. Chemseddine, D. Friedrich and R. van de Krol,
23 *Chem. Mater.*, 2016, 28, 4231-4242, <https://doi.org/10.1021/acs.chemmater.6b00830>.

24 12. Y. Xu, J. Jian, F. Li, W. Liu, L. Jia and H. Wang, *J. Mater. Chem. A*, 2019, 7, 21997-22004,
25 <https://doi.org/10.1039/c9ta07892d>.

26 13. S. Wei, N. Xu, F. Li, X. Long, Y. Hu, L. Gao, C. Wang, S. Li, J. Ma and J. Jin,
27 *ChemElectroChem*, 2019, 6, 3367-3374, <https://doi.org/10.1002/celc.201900714>.

28 14. N. W. Kim, B. U. Choi, H. Yu, S. Ryu and J. Oh, *Opt. Express*, 2019, 27, A171-A183,
29 <https://doi.org/10.1364/OE.27.00A171>.

30 15. T. Chtouki, M. El Mrabet, A. Tarbi, I. Goncharova and H. Erguig, *Opt. Mater.*, 2021, 118,
31 111294, <https://doi.org/10.1016/j.optmat.2021.111294>.

32 16. J. Yu, W. Han, A. A. Suleiman, S. Han, N. Miao and F. C. Ling, *Small Methods*, 2024, 8,
33 2301282, <https://doi.org/10.1002/smtb.202301282>.

1 17. J. Lee, H. Yoon, S. Kim, S. Seo, J. Song, B. U. Choi, S. Y. Choi, H. Park, S. Ryu, J. Oh
2 and S. Lee, *Chem. Commun.*, 2019, 55, 12447-12450, <https://doi.org/10.1039/c9cc06092h>.
3 18. R. Garg, S. Gonuguntla, S. Sk, M. S. Iqbal, A. O. Dada, U. Pal and M. Ahmadipour, *Adv.*
4 *Colloid Interface Sci.*, 2024, 330, 103203, <https://doi.org/10.1016/j.cis.2024.103203>.
5 19. B. Dupoyer, C. Tenailleau, Y. Thimont, P. Lenormand, A. Barnabé and L. Presmanes,
6 *Mater. Res. Bull.*, 2020, 130, 110940, <https://doi.org/10.1016/j.materresbull.2020.110940>.
7 20. S. Shahidi, B. Moazzenchi and M. Ghoranneviss, *Eur. Phys. J. Appl. Phys.*, 2015, 71, 31302,
8 <https://doi.org/10.1051/epjap/2015140439>.
9 21. B. Meena, M. Kumar, R. K. Hocking, S. Juodkazis, V. Biju, P. Subramanyam and C.
10 Subrahmanyam, *Energy Fuels*, 2023, 37, 14280-14289,
11 <https://doi.org/10.1021/acs.energyfuels.3c00731>.
12 22. F. C. Krebs, *Sol. Energy Mater. Sol. Cells*, 2009, 93, 394-412,
13 <https://doi.org/10.1016/j.solmat.2008.10.004>.
14 23. F. Wang, A. Chemseddine, F. F. Abdi, R. van de Krol and S. P. Berglund, *J. Mater. Chem. A*, 2017, 5, 12838-12847, <https://doi.org/10.1039/c7ta03009f>.
15 24. D. Perednis and L. J. Gauckler, *J. electroceram.*, 2005, 14, 103-111,
16 <https://doi.org/10.1007/s10832-005-0870-x>.
17 25. T. H. V. Nguyen, C.-H. Wu, S.-Y. Lin and C.-Y. Lin, *J. Taiwan Inst. Chem. Eng.*, 2019,
18 95, 241-251, <https://doi.org/10.1016/j.jtice.2018.07.010>.
19 26. C.-Y. Lin, S.-Y. Lin, M.-C. Tsai and C.-H. Wu, *Sustain. Energy Fuels*, 2020, 4, 625-632,
20 <https://doi.org/10.1039/c9se00558g>.
21 27. N. T. Hahn, V. C. Holmberg, B. A. Korgel and C. B. Mullins, *J. Phys. Chem. C*, 2012, 116,
22 6459-6466, <https://doi.org/10.1021/jp210130v>.
23 28. E. Kalinina and E. Pikalova, *Materials*, 2021, 14, 5584,
24 <https://doi.org/10.3390/ma14195584>.
25 29. Y. Nakabayashi, M. Nishikawa and Y. Nosaka, *Electrochim. Acta*, 2014, 125, 191-198,
26 <https://doi.org/10.1016/j.electacta.2014.01.088>.
27 30. A. Al-Osta, B. S. Samer, U. T. Nakate, V. V. Jadhav and R. S. Mane, *Microelectronic
Engineering*, 2020, 229, 111359, <https://doi.org/10.1016/j.mee.2020.111359>.
28 31. M. G. Weldehans, T. T. K. Ngan, T. T. Salunkhe and I. T. Kim, *J. Mater. Chem. A*, 2025,
29 DOI: 10.1039/d5ta07895d, <https://doi.org/10.1039/d5ta07895d>.
30 32. H.-S. Kim, R. Verma, J. Kim and C.-J. Park, *ACS Sustainable Chem. Eng.*, 2020, 8, 11123-
31 11132, <https://doi.org/10.1021/acssuschemeng.0c01513>.
32 33. S. M. Paradine, *Tetrahedron*, 2025, 184, <https://doi.org/10.1016/j.tet.2025.134781>.
33 34

1 34. D. Piecha, J. Kapusta-Kołodziej, M. M. Marzec, K. Sokołowski, M. Kozieł and A. Brzozka
2 *Appl. Surf. Sci.*, 2025, 713, 164330, <https://doi.org/10.1016/j.apsusc.2025.164330>.

3 35. T. Wu, J. Kim, Y. H. Choa and N. V. Myung, *Front. Chem.*, 2025, 13, 1635084,
4 <https://doi.org/10.3389/fchem.2025.1635084>.

5 36. M. Alhabradi, S. Nundy, A. Ghosh and A. A. Tahir, *ACS Omega*, 2022, 7, 28396-28407,
6 <https://doi.org/10.1021/acsomega.2c02996>.

7 37. M. Alruwaili, A. Roy, S. Nundy and A. A. Tahir, *RSC Adv.*, 2022, 12, 34640-34651,
8 <https://doi.org/10.1039/d2ra05894d>.

9 38. L. Zhao, X. Wang and Z. Liu, *Appl. Phys. A*, 2018, 124, 836,
10 <https://doi.org/10.1007/s00339-018-2262-5>.

11 39. J. Lee, H. Yoon, K. S. Choi, S. Kim, S. Seo, J. Song, B. U. Choi, J. Ryu, S. Ryu, J. Oh, C.
12 Jeon and S. Lee, *Small*, 2020, 16, e2002429, <https://doi.org/10.1002/smll.202002429>.

13 40. K.-H. Park and M. Dhayal, *RSC Adv.*, 2015, 5, 33503-33514,
14 <https://doi.org/10.1039/c4ra15704d>.

15 41. K. D. Malviya, H. Dotan, D. Shlenkevich, A. Tsyanok, H. Mor and A. Rothschild, *J.
16 Mater. Chem. A*, 2016, 4, 3091-3099, <https://doi.org/10.1039/c5ta07095c>.

17 42. O. Ait Layachi, A. Moujib and E. m. Khoumri, *Electroanal.*, 2024, 36,
18 <https://doi.org/10.1002/elan.202400115>.

19 43. J. Lin, M. Kilani, M. Baharfar, R. Wang and G. Mao, *Nanoscale*, 2024, 16, 19564-19588,
20 <https://doi.org/10.1039/d4nr02389g>.

21 44. X. Wang, W. Liu, C. Wang, S. Zhang, M. Ding and X. Xu, *Sens. Actuators B: Chem.*, 2021,
22 344, 130190, <https://doi.org/10.1016/j.snb.2021.130190>.

23 45. F. Wang, H. Yang and Y. Zhang, *Mater. Sci. Semicond. Process.*, 2018, 73, 58-66,
24 <https://doi.org/10.1016/j.mssp.2017.09.029>.

25 46. J. Wang, L. Tang, G. Zeng, Y. Liu, Y. Zhou, Y. Deng, J. Wang and B. Peng, *ACS
26 Sustainable Chem. Eng.*, 2016, 5, 1062-1072, <https://doi.org/10.1021/acssuschemeng.6b02351>.

27 47. S. Yu, H. Huang, F. Dong, M. Li, N. Tian, T. Zhang and Y. Zhang, *ACS Appl. Mater.
28 Interfaces*, 2015, 7, 27925-27933, <https://doi.org/10.1021/acsami.5b09994>.

29 48. J. Ghijssen, L. H. Tjeng, J. van Elp, H. Eskes, J. Westerink, G. A. Sawatzky and M. T.
30 Czyzyk, *Phys. Rev. B*, 1988, 38, 11322-11330, <https://doi.org/10.1103/physrevb.38.11322>.

31 49. HarwellXPS, HARWELLXPS GURU,
32 <https://www.harwellxps.guru/xpskb/copper/#1755794343725-850aad2-863d>, (accessed 10th
33 September, 2025).



1 50. M. C. Biesinger, *Surf. Interface Anal.*, 2017, 49, 1325-1324. View Article Online
DOI: 10.1002/sia.6239

2 <https://doi.org/10.1002/sia.6239>.

3 51. M. C. Biesinger, L. W. M. Lau, A. R. Gerson and R. S. C. Smart, *Appl. Surf. Sci.*, 2010,
4 257, 887-898, <https://doi.org/10.1016/j.apsusc.2010.07.086>.

5 52. L. Qu, R. Tan, A. Sivanantham, M. J. Kang, Y. J. Jeong, D. H. Seo, S. Kim and I. S. Cho,
6 *J. Energy Chem.*, 2022, 71, 201-209, <https://doi.org/10.1016/j.jecchem.2022.03.013>.

7 53. S. Sharma and N. Khare, *Colloid Polym. Sci.*, 2018, 296, 1479-1489,
8 <https://doi.org/10.1007/s00396-018-4362-3>.

9 54. F. Wang, W. Septina, A. Chemseddine, F. F. Abdi, D. Friedrich, P. Bogdanoff, R. van de
10 Krol, S. D. Tilley and S. P. Berglund, *J. Am. Chem. Soc.*, 2017, 139, 15094-15103,
11 <https://doi.org/10.1021/jacs.7b07847>.

12 55. M. Li, X. Tian, X. Zou, X. Han, C. Du and B. Shan, *Int. J. Hydrot. Energy*, 2020, 45,
13 15121-15128, <https://doi.org/10.1016/j.ijhydene.2020.03.242>.

14 56. N. Hoang Lam, N. Tam Nguyen Truong, K.-S. Ahn, Y. Jo, S. Beom Kang, N. Huu Hieu,
15 S. F. Shaikh, C.-D. Kim, M. Lee and J. Hak Jung, *FlatChem*, 2024, 43, 100600,
16 <https://doi.org/10.1016/j.flatc.2023.100600>.

17 57. S. Huang, G. Wang, J. Liu, C. Du and Y. Su, *ChemCatChem*, 2020, 12, 4431-4445,
18 <https://doi.org/10.1002/cctc.202000634>.

19 58. A. Kudo and Y. Miseki, *Chem. Soc. Rev.*, 2009, 38, 253-278,
20 <https://doi.org/10.1039/b800489g>.

21 59. M. Mouanga, L. Ricq and P. Berçot, *J. Appl. Electrochem.*, 2007, 38, 231-238,
22 <https://doi.org/10.1007/s10800-007-9430-1>.

23 60. S. Survilienė, O. Nivinskienė, A. Češunienė and A. Selskis, *J. Appl. Electrochem.*, 2006,
24 36, 649-654, <https://doi.org/10.1007/s10800-005-9105-8>.

25 61. W. Xue, J. Tian, X. Hu, J. Fan, T. Sun and E. Liu, *Chem. Eng. J.*, 2022, 443, 136427,
26 <https://doi.org/10.1016/j.cej.2022.136427>.

27 62. S. Zhang, M. Rohloff, O. Kasian, A. M. Mingers, K. J. J. Mayrhofer, A. Fischer, C. Scheu
28 and S. Cherevko, *J. Phys. Chem. C*, 2019, 123, 23410-23418,
29 <https://doi.org/10.1021/acs.jpcc.9b07220>.

30 63. M. G. De Chialvo, J. Zerbino, S. Marchiano and A. Arvia, *J. appl. electrochem.*, 1986, 16,
31 517-526, <https://doi.org/10.1007/BF01006847>.

32 64. H. Khan, M.-J. Kim, P. Balasubramanian, M.-J. Jung and S.-H. Kwon, *Cell Rep. Phys. Sci.*,
33 2023, 4, 101652, <https://doi.org/10.1016/j.xcrp.2023.101652>.

34

Data availability

[View Article Online](#)
DOI: 10.1039/D5MA01065A

All data supporting the findings of this study are included within the article and its Electronic Supplementary Information (ESI).